Correcting for water vapor diffusion in air bag samples for isotope composition analysis: case study with drone-collected samples

Di Wang[1,2,3*], Camille Risi[2], Lide Tian[1], Di Yang[1], Gabriel J. Bowen[4], Siteng Fan[2,5],

Yang Su[6] , Hongxi Pang[7], Laurent Z.X Li[2]

[1] Institute of International Rivers and Eco-security, Yunnan University, Yunnan Key Laboratory of International Rivers and Transboundary Eco–security, Kunming 650500, Yunnan, China

[2] Laboratoire de Météorologie Dynamique, IPSL, CNRS, Sorbonne Université, Campus Pierre et Marie Curie, Paris 75005, France

[3] Laboratoire Atmosphères, Observations Spatiales, IPSL, CNRS, UVSQ, Sorbonne Université, Guyancourt 78280, France

[4] Department of Geology and Geophysics, University of Utah, Salt Lake City, Utah 84108, USA

[5] Department of Earth and Space Sciences, Southern University of Science and Technology, Shenzhen 518055, China

[6] Département d'Informatique, École normale supérieure – PSL, 45 Rue d'Ulm, 75005 Paris, France

[7] Key Laboratory of Coast and Island Development of Ministry of Education, School of Geography and Ocean Science, Nanjing University, Nanjing 210023, China

*Corresponding author: di.wang@latmos.ipsl.fr; shidi.upmc@gmail.com

Abstract

Mass spectrometry and laser spectroscopy have been widely employed for precise water vapor isotope measurements. Nevertheless, these techniques are limited by logistical challenges in fieldwork, consequently constraining the temporal and spatial resolution of measurements. Specifically, water vapor isotope measurements are primarily limited to near-surface levels, while measurements in the free troposphere are notably scarce. Portable sampling devices, such as air bags and glass bottles, have therefore become necessary alternatives for collecting, storing, and transporting gaseous samples in diverse environments prior to analysis with less portable instruments. In drone-based high-altitude vapor sampling, air bags are preferred for their lighter weight and greater flexibility compared to glass bottles. Nevertheless, they present specific challenges, such as potential sample contamination and isotopic fractionation during storage, primarily due to the inherent permeability of air bags. Here, we developed a theoretical model for water vapor diffusion through the sampling bag surface, with parameters calibrated through laboratory experiments. This model enables the reconstruction of the initial isotopic composition of sampled vapor based on measurements obtained within the bag and from the surrounding environment. This diffusion model underwent rigorous validation through experiments conducted under varying humidity and isotopic composition differences between the inside and outside of the air bag, confirming its reliability. We applied this correction method to air samples collected at various pressures up to the upper troposphere using an air bag-mounted drone that we developed, thereby estimating the initial isotopic composition and uncertainty based on our observations. Our correction method enhances the reliability and applicability of water vapor isotope observations conducted using drones equipped with air bags, and provides a detailed assessment of all potential sources of error and quantifies the uncertainty range of the observations. This approach leverages the strengths of drone-based air bag sampling while mitigating its limitations, thus facilitating the convenient collection of isotopic data throughout the troposphere.

1 Introduction

Water vapor isotopes provide unique insights into the transport, mixing, and phase changes of water in the environment, which are crucial for improving understanding of the climate system, hydrological cycle, atmospheric dynamics, and paleoclimate proxies. Water isotopes have also been applied in climate modeling, weather prediction, and water resource management (Bowen et al., 2019; Galewsky et al., 2016; Gat, 1996; West et al., 2009).

Water isotope analysis has traditionally relied on mass spectrometry, which, while accurate (Ghosh and Brand, 2003; Muccio and Jackson, 2009), demands labor-intensive preparation and lacks portability (West et al., 2010). Methods like cryogenic trapping effectively collect water vapor (Grootes and Stuiver, 1997; Michener and Lajtha, 2008; Steen-Larsen et al., 2011; Yu et al., 2015), but they require long sampling periods, limiting observation scope and timing. Over the past three decades, laser spectroscopy methods such as Cavity Ring-Down Spectroscopy (CRDS)(Hodges and Lisak, 2006) and Off-Axis Integrated Cavity Output Spectroscopy (OA-ICOS) (Johnson et al., 2011) have emerged, delivering a best-in-class combination of speed, high precision, and continuous measurements even in challenging environments such as high altitudes or arid regions with low water vapor content. Advances in these instruments have significantly expanded the field of water isotope research. However, their heavy instrumentation, substantial power requirements, and limited mobility restrict their usability in certain situations, particularly for aerial water vapor isotope measurements, which require lightweight and flexible sampling approaches. As a result, the collection and storage of physical samples are still necessary, increasing the demand for more convenient and efficient sample acquisition methods. Air bags and glass bottles have been practical solutions for collecting, storing, and transporting gaseous samples from various settings (Rozmiarek et al., 2021).

Given that air bags can reduce the weight of sampling equipment and increase sampling flexibility, there is considerable interest in using them for vapor sample collection. This is particularly advantageous for small equipment like drones, where minimizing payload weight is essential for sampling at high altitudes or over long distances. This selection also makes it easier to transport samples and reduces the risk of breakage. However, concerns have arisen regarding the suitability of various sampling materials for storing these samples, primarily due to potential water diffusion through container walls. Diffusion issues are commonly observed in sampling bags during water vapor isotope analysis and have persisted as a longstanding challenge in the field (Gralher et al., 2021; Havranek et al., 2020; Herbstritt et al., 2023; Magh et al., 2022). In previous studies, this issue is particularly concerning in the Direct Vapor Equilibrium Laser Spectroscopy (DVE-LS) method, which has been widely used to rapidly collect and measure water isotopes in evaporation-prone soil, rock, or plant samples. The DVE-LS method simplifies preparation and increases sample throughput by directly analyzing the vapor phase, thus eliminating the need for extensive physical extractions (Gralher et al., 2021; Hendry et al., 2015; Millar et al., 2018; Sprenger et al., 2015; Wassenaar et al., 2008). However, water vapor molecules may exchange between the air inside the bag and the external ambient air during sample storage. Water vapor molecules typically diffuse from areas of high humidity to drier areas. In this process, heavier isotopologues (e.g., $H_2^{18}O$ and HDO) move more slowly than lighter isotopologues (e.g., $H_2^{16}O$) due to their greater mass, resulting in preferential

diffusion of lighter isotopes. This differential diffusion, can alter the original isotopic composition of the collected air samples. Moreover, differential diffusion can also occur due to gradients in isotopic composition.

To mitigate these issues, specific diffusion-tight materials are highly recommended for water vapor isotope measurements, although adsorption effects may still occur with such materials(Herbstritt et al., 2023). Further research and development are still necessary. This may involve exploring alternative materials for more impermeable sampling bags, improving sealing methods to better isolate sampled air, and developing sampling techniques less susceptible to diffusion. Resolving these issues is essential for ensuring the reliability of water vapor isotope measurements using air bags and for accurately understanding atmospheric and hydrological processes.

In light of the ongoing development and further refinement of these techniques and the associated cost constraints, we developed a diffusion model with parameters calibrated through laboratory experiments. This model is capable of assessing the permeability of the air bags and correcting the obtained isotope measurements to the initial pre-diffusion values based on the humidity, isotope values inside and outside the bag, and the sample storage time. This diffusion model was validated through experiments under varying humidity and isotopic composition differences between the inside and outside of the air bag, confirming its reliability. Furthermore, we also applied this diffusion method to air samples collected at different altitudes using a drone-based atmospheric vapor sampling device we developed, to estimate the initial isotope composition and uncertainty. The primary objective of this drone-based field campaign is to obtain atmospheric water vapor isotope data along vertical profiles in the troposphere, providing higher temporal and spatial resolution than satellite observations. The corrected near-surface drone-based measurements using our diffusion model show improved consistency with direct, in-situ surface-level measurements using the Picarro analyzer. Our model, validated by laboratory experiments under a wide range of environmental conditions, was used to assess all potential error sources and to quantify a conservative, comprehensive uncertainty range for the corrected vertical profiles. Although we minimized certain diffusion-related biases, such as pressure in different altitudes and long storage times, temperature and the pressure difference between the inside and outside of the bags on bag permeability were only addressed indirectly via conservative uncertainty estimates. This treatment is justified under our experimental conditions, which are characterized by the short residence time at high altitudes, the reduced diffusivity at low temperatures, and the flexibility of the bags maintaining equal internal and external pressure. Future applications should consider the specific experimental conditions, and future developments may extend the model to explicitly incorporate the dependence of bag permeability on partial pressure and temperature, thereby improving its applicability under a wider range of atmospheric conditions.

2 Theoretical basis of diffusion model

2.1 Diffusion model description

Storing vapor samples in air bags prior to isotope measurement may alter the isotopic

131   composition of the water vapor. The main reason is the diffusion of water molecules between
132   the interior and exterior of the air bags, primarily due to the permeability of the bag materials.
133   We present a mathematical model for the diffusion and fractionation of isotopes across the
134   surface of the sampling bag. In this model, we assume the ambient vapor flux entering the air
135   bag changes the internal humidity and vapor isotopic composition, influenced by the different
136   humidity and water isotopic composition inside and outside the bag (Fig.1).

137   The flux of water into the bag, F (in $kg/m^2/s$), is expressed as:

138       $$F = k * (q_e - q(t)) \tag{1}$$

139   where $q(t)$ represents the variation of humidity inside the air bag over time (in kg/kg), q_e
140   denotes the environmental humidity (in kg/kg), k is water vapor conductance. This first-order
141   formulation is derived from Fick's diffusion law(Fick, 1855).

142   Similarly, the flux of isotopologue, F_i, either $H_2^{18}O$ or HDO, moving into the bag can be
143   described as:

144       $$F_i = k_i * (R_e * q_e - R(t) * q(t)) \tag{2}$$

145   In this equation, k_i represents the conductance specific to each isotopologue (in $kg/m^2/s$), R_e
146   denotes the isotopic ratio in the environment, and $R(t)$ is the variation of isotopic ratio within
147   the air bag with time. Notably, the fractionation coefficient here can be denoted as:

148       $$\alpha = \frac{k}{k_i} \tag{3}$$

149   Since k represents the total conductance dominated by the lighter molecules ($H_2^{16}O$), and k_i
150   is defined as the conductance of the heavier isotopologues (either $H_2^{18}O$ or HDO), Eq. (3) is
151   therefore consistent with the conventional definition of fractionation factors ($\alpha = k_{light}/k_{heavy}$).

152   The validity of Eqs.1 and 2 relies on the assumptions that internal and external pressures
153   remain equal to atmospheric pressure, ensuring no pressure gradient across the bag membrane,
154   that the internal vapor is well-mixed, and that the exchange rate follows a first-order process.
155   Additionally, if the temperature remains constant, k and k_i are assumed to be constant.

156

157   Assuming that diffusion through the bag is the primary transport mechanism, and
158   neglecting adsorption, the temporal change in humidity can be modeled by the following
159   differential equation:

160       $$\frac{d(q(t)*M)}{dt} = F * A \tag{4}$$

161   where A represents the exchange area (surface area of the air bag), and M is the air mass
162   inside the bag.

163   Assuming that M is constant, which is reasonable given that the total mass variation due
164   to water vapor flux is at most 1%, this equation simplifies to:

165       $$\frac{dq(t)}{dt} = \frac{F*A}{M} = \frac{k*A}{M} * (q_e - q(t)) \tag{5}$$

166   Here, we define the water vapor exchange coefficient as follows, it describes the rate at
167   which water vapor exchanges across the bag membrane:

168       $$\lambda = \frac{k*A}{M} \tag{6}$$

169   Similarly, the temporal change in isotopic ratio can be modeled by the following
170   differential equation:

171
$$\frac{d(R(t)*q(t)*M)}{dt} = M * (q(t) * \frac{dR(t)}{dt} + R(t) * \frac{dq(t)}{dt})$$

172
$$= F_i * A = k_i * (R_e * q_e - R(t) * q(t)) * A \tag{7}$$

173   This equation can be simplified as:

174
$$\frac{dR(t)}{dt} = \frac{ki * (R_e * q_e - R(t)*q(t)) * A/M - R(t) * \frac{dq(t)}{dt}}{q(t)}$$

175
$$= \frac{\frac{k*A}{M*\alpha} * (R_e * q_e - R(t)*q(t)) - R(t) * \frac{k*A}{M} * (q_e - q(t))}{q(t)}$$

176
$$= \frac{\frac{\lambda}{\alpha} * (R_e * q_e - R(t)*q(t)) - R(t) * \lambda * (q_e - q(t))}{q(t)}$$

177
$$= \frac{\lambda}{\alpha} * (R_e - R(t)) + \frac{\lambda}{q(t)} * (q_e - q(t)) * (\frac{R_e}{\alpha} - R(t)) \tag{8}$$

178

179   If q_e is stable (the environment is treated as an infinite reservoir), and that k and A are
180   constant, the differential equation for humidity (Eq. 5) can be analytically solved:

181
$$q_e - q(t) = (q_e - q_0) * e^{(-\frac{k*A}{M}*t)} = (q_e - q_0) * e^{(-\lambda*t)} \tag{9}$$

182   where q_0 is the initial humidity at $t = 0$. This equation can also be expressed in terms of
183   natural logarithms as:

184
$$\ln (q_e - q(t)) = \ln (q_e - q_0) - \lambda * t \tag{10}$$

185   Consequently, the slope of $\ln (q_e - q(t))$ against time is λ.

186

187   For the isotopic ratio, the analytical solution is only feasible when the initial humidity
188   equals the environmental humidity ($q_0 = q_e$):

189
$$\frac{dR(t)}{dt} = \frac{k*A}{M*\alpha} * (R_e - R(t)) \tag{11}$$

190   Assuming that R_e, q_e, k, α and A are constant:

191   Thus,
$$R_e - R(t) = (R_e - R_0) * e^{(-\frac{k*A}{M*\alpha}*t)} \tag{12}$$

192   where R_0 denotes the initial isotopic ratio at $t = 0$. Again, taking the natural logarithm, we
193   obtain:

194
$$\ln (R_e - R(t)) = \ln (R_e - R_0) - \frac{\lambda}{\alpha} * t \tag{13}$$

195   This equation demonstrates that the slope of $\ln (R_e - R(t))$ against time is the water vapor

196   isotopic exchange coefficient $\frac{\lambda}{\alpha}$. Knowing λ, we can deduce the isotopic fractionation

197   coefficient α for each isotope.

198   However, when the environmental humidity differs from the initial humidity inside the air
199   bag, a numerical solution is required to solve the differential equation for R (Eq. 8).

$q_0 < q_e$

Water vapor
exchange coefficient:
$\lambda = \frac{k*A}{M}$

q_e

Isotopic exchange
coefficient:
$\frac{k*A}{M*\alpha} = \frac{\lambda}{\alpha}$

δ_e

q_0

R_0

Air bag   Environment
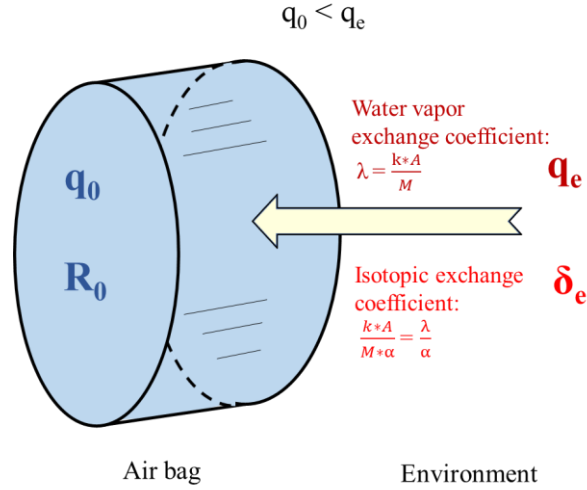
Figure 1 Schematic illustrating the diffusion model. q_0 represents the initial humidity in the air bag at t = 0, q_e denotes the environmental humidity, R_0 indicates the initial isotopic ratio in the air bag at t = 0, R_e represents the isotopic ratio in the environment, k is water vapor conductance, A denotes the exchange area (surface area of the bag), and M is the mass of air within the bag, and α denotes the isotopic fractionation coefficient.

2.2 **Reconstructing initial water vapor isotopic compositions**

The isotopic composition of the air bag water vapor undergoes an exponential evolution over time (Eq. 12). This method of applying exponential evolution equations to reconstruct isotopic compositions has been used in environmental forensics to investigate shifts in water isotopes due to metabolic changes, environmental conditions, or diet (Ayliffe et al., 2004; Cerling et al., 2006). Similarly, in climatology, this method helps retrieving initial isotopic composition from samples such as ice cores or tree rings, affected by evaporation, precipitation, and temperature fluctuations, facilitating historical climate reconstruction (Brienen et al., 2016). Here we apply a similar method, and apply the analytical solution of Eq. 8 using data from experiments in which the condition that q_0 equals q_e is met to determine the equation parameters.

The constants (λ, $\alpha^{18}O$, α^2H) can be determined through laboratory experiments and Eqs. 10 and 13 (see Subsection 3.2 and 4.1). If we know the initial values within the air bag (q_0, $R^{18}O_0$, R^2H_0), the ambient values (q_e, $R^{18}O_e$, R^2H_e) during storage (approximated using ground-level conditions), and the storage time after sampling ($T_{storage}$), we are able to simulate the variations in humidity and isotopic ratios inside the air bag according to Eqs. 5 and 8. Similarly, if we know $T_{storage}$, the humidity and isotopic composition at time t = $T_{storage}$ ($q_{(Tstorage)}$, $R^{18}O_{(Tstorage)}$, $R\_^2H_{(Tstorage)}$ in the air bag, and the ambient values, we can deduce the initial values in the air bag at t = 0 by back-calculating. The equation used for reconstructing the initial isotope ratio (R_0) is:

$$R_0 = R_{measured} - \int_0^{T_{storage}} \frac{dR(t)}{dt} dt$$

$$= R_{measured} - \int_0^{T_{storage}} (\frac{\lambda}{\alpha} * (R_e - R(t)) + \frac{\lambda}{q(t)} * (q_e - q(t)) * (\frac{R_e}{\alpha} - R(t))) \, dt \qquad (14)$$

where R_0 represents the initial isotopic ratio to be reconstructed, $R_{measured}$ is the observed

223   isotopic ratio after $T_{storage}$, and $\frac{dR(t)}{dt}$ is defined in Eq. 8.

224   This approach allows us to correct for diffusion-induced isotopic shifts and reconstruct the
225 original vapor composition.

226   For mathematical clarity and consistency, isotopic ratios (R) are used in the equations
227 presented in previous sections. Replacing R with δ-values would only shift the physical basis
228 without affecting the mathematical validity of the equations or the estimation of α, as the
229 standard ratio cancels out. For clearer visualization, δ-values are used for numerical
230 applications and in the subsequent figures and tables.

231   The δ and d-excess values used in this study follow standard definitions:

232 $$\delta^{18}O = \left(\frac{R^{18}O_{sample}}{R^{18}O_{standard}} - 1 \right) * 1000 \qquad (15)$$

233 $$\delta^{2}H = \left(\frac{R^{2}H_{sample}}{R^{2}H_{standard}} - 1 \right) * 1000 \qquad (16)$$

234 $$d - excess = \delta^{2}H - 8 * \delta^{18}O \qquad (17)$$

235   Here, $R^{18}O_{standard} = 2.0052*10^{-3}$ and $R^{2}H_{standard} = 1.5576 * 10^{-4}$, corresponding to
236 the VSMOW international reference values.

3   Methods and data

3.1   Air bag isotope measurements
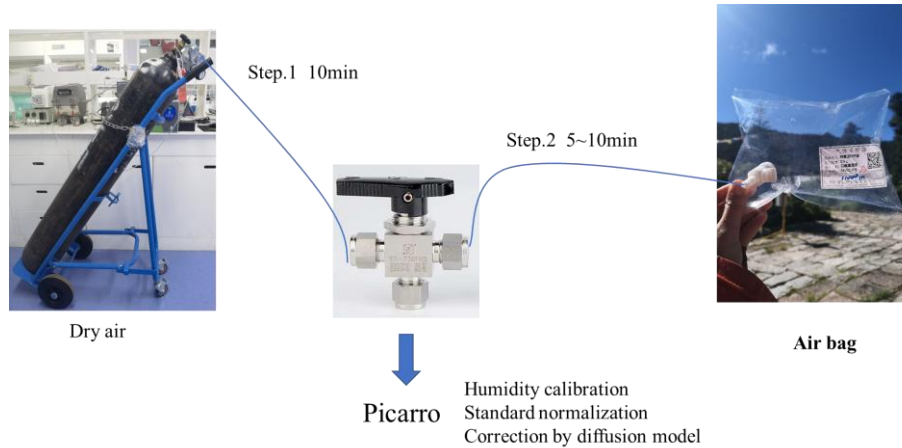
*Figure 2 Setup for isotope measurements using air bags with a Picarro atmospheric
water vapor isotope analyzer.*

239   In this study, we used 0.5 L and 4 L Teflon air bags produced by Dalian Hede Technologies
240 Co., Ltd to collect and store vapor, and measured the vapor isotopes using a Picarro 2130i water
241 isotope analyzer. Based on our testing and the airflow rate set for the Picarro analyzer, the 0.5
242 L and 4 L bags provided sufficient sample volume for approximately 17 minutes and 130
243 minutes of analysis, respectively.

Figure 2 illustrates the setup for measuring vapor isotopes in air bags. In this system, the air inlet of the Picarro isotope analyzer was connected to a three-way valve through Teflon or stainless-steel tubing. The other two ports of the three-way valve were attached to the outlet valve of the air bag and a dry air cylinder, respectively. Sample storage and measurement were conducted in a temperature-regulated room to maintain constant temperature conditions for the air bags and tubing.

In the measurement procedure, we first activated the dry air cylinder and adjusted the pressure reducing valve to 13.8 kPa (2 psi, pounds of force per square inch), within the Picarro water isotope analyzer's recommended range of 13.8–27.6 kPa (2–4 psi) for carrier gas. The instrument's built-in flow regulation maintains a gas flow rate of 40 sccm at 760 Torr, corresponding to ~ 30–50 mL/min in our measurement conditions, ensuring stable sample delivery. We then opened the valve channel connecting the dry air cylinder to the three-way valve, allowing dry air to flow into the isotope analyzer and flush all air pathways for 10 minutes. Subsequently, we closed the dry air channel, opened the air bag outlet valve, and the corresponding valve channel on the three-way valve. This allowed water vapor in the air bags to be analyzed at a constant temperature in the Picarro analyzer, a process lasting between 5 and 10 minutes. Upon completion, we switched the valve to measure dry air. By repeatedly measuring isotopic composition for replicate samples—air samples collected simultaneously under the same conditions—we ensured the consistency of the water vapor measurements.

To correct isotope measurement bias caused by the instrument's sensitivity to different water vapor concentrations(Schmidt et al., 2010), we used the built-in Standard Delivery Module (SDM) of the Picarro L2130-i water vapor isotope analyzer to generate a 500–25,000 ppm water vapor gradient for isotope measurements. We selected 20,000 ppm as a reference humidity level, as this corresponds to the optimal accuracy range of the Picarro analyzer (JingfengLiu et al., 2014; Schmidt et al., 2010). All the measured vapor isotope data were normalized to the VSMOW-SLAP scale using two distinct laboratory reference waters with known isotopic composition. Before conducting daily measurements, we adjusted the quantity of the injected liquid standard to align with the humidity of the external vapor measurements.

3.2 **Laboratory permeability experiments**

To evaluate the variations of the diffusion of water molecules between the interior and exterior of the air bags, we conducted the following experiments (Table A1), as detailed below:

3.2.1 **Experiment No. 1: Quantification of $\lambda_{surface}$**

To quantify the water vapor exchange coefficient at the surface, $\lambda_{surface}$, using Eq.10, we filled the empty and clean air bags with dry air and measured humidity variations using a Picarro analyzer at intervals of 1 minute, 2, 4, 6, 8, and 10 hours following the measurement method described in Subsection 3.1. As λ is related to the surface area of the sampling bag, measurements were conducted using 0.5L and 4L air bags, with repetitions on both identical and different air bags of the same dimensions (refer to the experiment times in Table 1 and results in Fig.3a). We measured $\lambda_{surface}$ (=k*A/M) under near-surface pressure and temperature we set in a controlled chamber. While k may vary with temperature and pressure, these effects

284 were assumed negligible within the condition of our study. Results will be shown in Subsection
285 4.1.

3.2.2 Experiment No. 2: Quantification of α

287 To investigate isotope variation patterns and improve measurement accuracy during
288 storage in the air bag to quantify the isotopic fractionation coefficient α, using Eq.13, initial
289 values significantly different from ambient conditions were selected. Empty, clean air bags
290 were first filled with dry air, then sealed by closing the bag valve. To maintain a closed system
291 while injecting reference water, a dedicated injection septum was installed on the valve. After
292 reopening the valve, a fixed amount of laboratory reference liquid water with known isotopic
293 composition was injected into the dry air-filled bag using a 10 μL injection needle. In
294 Experiment No. 2, we ensured that the initial humidity (q_0) was approximately equal to the
295 environmental humidity (q_e). To ensure $q_0 = q_e$, the environmental vapor concentration was first
296 measured, followed by the calculation and experimental determination of the water volume to
297 be injected into the air bag. Water vapor concentration and isotope variations within the air bags
298 were then measured using a Picarro analyzer at intervals of 5 minutes, 2, 4, 6, 8, and 10 hours.
299 Results will be shown in Subsection 4.1. To ensure data consistency and reliability, we repeated
300 these measurements multiple times using air bags of both the same and different sizes, including
301 0.5L and 4L bags. For the 0.5L air bags, a separate bag was prepared for each time interval, and
302 water vapor concentration and isotopic compositions were measured once to ensure that the
303 parameter M remained stable without being affected by repeated measurements. However,
304 manual injection of reference water with known isotopic composition introduced some
305 variability, causing minor variations in initial values across all bags. This is evident in Figs 5,
306 6, and A2, where $q_0 = 1/2\, q_e$ data exhibit slight fluctuations due to the use of separate bags for
307 each time interval. To address this, we repeated the experiment with 4L air bags, measuring the
308 same air bag at different time intervals, which ensured consistent initial conditions at t=0 but
309 allowed M to change over time. When air bags differ only in size, the parameter λ associated
310 with A and M varies, while the isotopic fractionation coefficient α is theoretically constant.
311 Both approaches could contribute to uncertainties in the mismatches between the model and
312 experimental results. Therefore, we incorporated the results from both the 0.5 L and 4 L
313 experiments into our uncertainty estimation of these mismatches, as detailed in Subsections
314 3.2.3 and 3.4.2.

3.2.3 Experiment No. 3: Diffusion model validation

316 To validate the diffusion model under diverse conditions and evaluate its uncertainties, we
317 repeated Experiment No. 2, but injected different amounts of water with known isotopic
318 composition to achieve a range of humidities from approximately $1/8 * q_e$ to q_e. Using the
319 method described in Experiment No. 2, we injected 6 to 50 μL of reference water into a 4L air
320 bag filled with dry air to achieve the desired humidity range. Additionally, we repeated the
321 experiment using two reference waters with distinct isotopic compositions, specifically $\delta^{18}O =$
322 -58.07‰, $\delta^2H = -447.41$‰ and $\delta^{18}O = -29.84$‰, $\delta^2H = -222.84$‰. To assess extended-duration
323 variations, we also lengthened the time interval to 24 hours.

Once the parameters of the diffusion model have been obtained through Experiments No. 1 and 2, we used this model to simulate the variations in water vapor humidity and isotopic composition inside the air bag over time for Experiments No. 2 and 3 (refer to Section 2). When simulating these experiments using the diffusion model, we used measurements taken after a 5-minute delay as the initial condition to ensure that it represented complete evaporation of the injected water. We then simulated the temporal variations in humidity and vapor isotopes within the air bag using a 5-minute time step using Eqs.5 and 8, separately. The resulting outputs (hereafter referred to as 'the diffusion model simulations') will be shown in Subsection 4.2 and code are available as supplementary material.

3.3 **Drone-mounted systems and field campaign**

We designed and built a collection module for fixed-height sampling, incorporating diaphragm vacuum pumps, a rudder mounted on the drone, and a control module linked to a remote operating system. Before flight, each air bag was evacuated on the ground using the diaphragm pumps. When inactive, these self-sealing pumps effectively isolated the interior of the air bags from the external environment, minimizing diffusion prior to sampling. When the drone reaches a specified altitude, we remotely activate the designated air pump to inflate a specific air bag. Once sampling is complete, the pump is deactivated, and the drone ascends to the next target altitude, where the corresponding air pump inflates another air bag. This process was repeated until all predetermined samples were collected. After each sampling, the pump remained sealed, ensuring no unintended air ingress during descent. Additionally, due to the flexible nature of the air bags, internal and external pressures remained balanced. As air pressure increases during the drone's descent after collection. To further prevent the loss of collected air samples, a one-way valve was installed to block backflow. Additionally, the one-way valve helps prevent large droplets from entering the air bag during the collection process.

The sampling module was mounted on our specially designed high-altitude drones and deployed during a field campaign conducted from June 25, 2020, to October 17, 2020, in the pristine forests of Mountain Laojun, Lijiang, on the southeastern edge of the Tibetan Plateau and the northwestern of the Yunnan-Guizhou Plateau, China. We collected water vapor samples every 500 meters, starting from near the surface along the vertical profile. To optimize sampling across different altitude ranges, we deployed UAVs designed for varying flight altitudes. Generally, the UAV operating at lower altitudes collected samples at seven heights from 4,000 to 7,000 meters in a single flight. The mid-altitude UAV collected samples at four heights from 7,500 to 9,000 meters in one flight, while the high-altitude UAV collected samples at four heights from 9,500 to 11,000 meters in two flights. Each flight took approximately 20~30 minutes. In case of any disruptions during sampling, we repeated the process until a complete vertical profile was obtained. At the beginning of the experiment, we also collected replicate samples at each height to ensure data consistency.

By integrating high-altitude drone sampling with subsequent water vapor isotope analysis using the Picarro analyzer at the surface, we obtained vapor isotopic profiles up to an altitude of 11 km. Unlike conventional methods, such as cryogenic vapor sampling, this approach requires much less sample volume and allows for timely measurements. Additionally, compared to large aircraft, airships, and balloon-based observations, this method is relatively low-cost

366 and supports more flexible and long-term observations.

3.4 **Application of diffusion model to vertical profiles**

3.4.1   **Estimating the air mass in the bag**

369   λ is defined as $k*A/M$ and depends on the air mass M in the bag. In drone-based vertical
370 sampling, M varies with altitude due to pressure changes, requiring an estimate of λ for different
371 altitudes (λ_{alt}). However, since λ is an intrinsic property of the bag material, its apparent
372 variation reflects uncertainties in estimating collected M, which depend on atmospheric
373 pressure (P), sampling time, and pump efficiency (ε):

374      $$M_{alt} = M_{surface} * \frac{P_{surface}}{P_{alt}} * \frac{\text{Sampling time}_{alt}}{\text{Sampling time}_{surface}} * \varepsilon \qquad (15)$$

375   where M_{alt} is the air mass collected at a different altitude and $M_{surface}$ represents the air mass
376 collected at the surface. At higher altitudes, where the air pressure (P_{alt}) is lower than at the
377 surface ($P_{surface}$), less air will be pumped into the air bag. To compensate for this effect, a longer
378 sampling time was used to collect air at higher altitudes (Sampling time$_{alt}$) than at the surface
379 (Sampling time$_{surface}$) (Fig.A1).
380   Given that λ_{alt} is proportional to M_{alt}, we calculated it as:

381      $$\lambda_{alt} = \lambda_{surface} * \frac{P_{surface}}{P_{alt}} * \frac{\text{Sampling time}_{alt}}{\text{Sampling time}_{surface}} * \varepsilon \qquad (16)$$

382   where $\lambda_{surface}$ is the λ quantified experimentally at the surface.
383   Since air pressure and sampling times were directly measured, the primary source of error
384 for M_{alt}, and consequently $\lambda_{alt,}$ arises from pump efficiency (ε), which may decrease over time
385 and at lower pressures. Using the estimated λ_{alt}, the observed vertical isotope profiles were
386 corrected based on Eq.14 from Section 2.2. The uncertainty estimation is discussed in Section
387 3.4.2.

3.4.2   **Method of uncertainty estimation**

389   Potential errors in correcting vertical profiles using the diffusion model include estimates
390 of $\lambda_{surface}$, α, pump efficiency (ε), and mismatches between model and experiments (Table 1).
391 We detail each below:
392   1) $\lambda_{surface}$ uncertainty: laboratory experiments provided upper and lower bounds on $\lambda_{surface}$
393 (Subsection 4.1). These were used for error estimation.
394   2) α uncertainty: the λ and λ/α were first estimated from several experiments, from which
395 α was calculated. Their averaged values were used separately to parameterize the model. As
396 highlighted in Subsection 3.2.2, estimating λ/α (and subsequently calculating α) requires results
397 from cases where q_0 equals q_e, minor variations in q_0 and fluctuations in q_e could introduce non-
398 systematic discrepancies between the model and experimental results. Consequently, for
399 analyzing the contribution of α to uncertainties, only α derived from experiments where the
400 model closely matched the majority of experimental results were considered. Selection criteria
401 for these experiments included minimal deviation between q_0 and q_e, minimal deviation

between experimental data and simulations, and stable q_e, ensuring the reliability of the chosen α.

3) Pump efficiency (ε) uncertainty: The efficiency of the pump may decline over time or vary with atmospheric pressure, affecting the collected air mass M. To account for this, we applied a conservative uncertainty range of 0.75 to 1.25 relative to surface conditions, ensuring the full range of possible variations in M_{alt} was considered.

4) Model-experiment mismatches: We compared model simulations with experimental data across 87 cases, calculating the average absolute discrepancy. These mismatches were included as an additional uncertainty component.

Total Uncertainty Calculation: The maximum discrepancy across all calibration results— using the full uncertainty range for $\lambda_{surface}$, α, and pump efficiency (ε)—was determined. The model-experiment mismatch was then added as an independent error component. The final uncertainty estimates, reported in Subsections 4.3 to 4.5, account for all potential error.

Table 1 Uncertainties and estimation methods

Uncertainties	Number of experiments	Estimation method	Used value (min~max for error estimation)
$\lambda_{surface}$	7 (0.5L bags); 6 (4L bags)	Obtained from lab experiments (max & min)	For 0.5L air bags: 0.031(0.0291~0.0317); For 4L air bags: 0.0255(0.0250~0.0259)
α	4	Obtained from lab experiments	$\alpha^{18}O$ is 1.0241, α^2H is 1.0451 ($\alpha^{18}O$ is 1.0254, α^2H is 1.0506 and $\alpha^{18}O$ is 1.0264, α^2H is 1.0380)
Pump efficiency (ε)	-	0.75~1.25 relative to surface conditions	0.75~1.25
Mismatches between model and experiments	87	Average of all differences between experimental data and simulations	0.5 ‰ for $\delta^{18}O$, 4.1 ‰ for δ^2H, 2.9 ‰ for d-excess

3.5 Satellite isotope data from IASI

Several satellite missions have contributed to water vapor isotope observations, including the Tropospheric Emission Spectrometer (TES) onboard Aura (2004–2018) (Worden et al., 2006), the Scanning Imaging Absorption Spectrometer for Atmospheric Cartography (SCIAMACHY) onboard Envisat (2002–2012), the Atmospheric Infrared Sounder (AIRS) onboard Aqua (since 2002) (Worden et al., 2019), and the Tropospheric Monitoring Instrument (TROPOMI) onboard Sentinel 5 Precursor (since 2017)(Schneider et al., 2020). In this study, we use the MUSICA retrievals from the Infrared Atmospheric Sounding Interferometer (IASI) onboard METOP due to its broad spatiotemporal coverage, vertical profiling capability, and the availability and accessibility of its dataset (Diekmann et al., 2021). It has a horizontal footprint of approximately 12 km at nadir (directly below the satellite), increasing with the angle of observation. This configuration ensures nearly global coverage twice daily.

In this study, as no satellite retrievals of $\delta^{18}O$ are currently available, we compared our observed vapor δ^2H profiles up to the upper troposphere with satellite observations. Due to the intermittent availability of IASI data at any given location, we limited our comparison of observational results across various altitudes at our study site to days when IASI data were available. Satellite measurements, particularly for vertical profiles of water vapor isotopes, are inherently different from direct sampling, they represent a vertical average over layers determined by the averaging kernels (Rodgers and Connor, 2003; Worden et al., 2006). Therefore, their comparability with ground-based or drone-based observations, which provide high-resolution local data, is limited. The MUSICA retrievals from the IASI satellite instrument provides water vapor isotope data at three altitude levels: 1-3 km in the lower troposphere, 4-7 km in the mid-troposphere, and 8-12 km in the upper troposphere. Given that our study started at an altitude of 3856 m, we used the retrieved δ^2H data for the 4–7 km and 8–12 km levels. However, these measurements represent a vertical average over layers determined by the

averaging kernels (Rodgers and Connor, 2003; Worden et al., 2006). While using averaging
kernels to smooth the observed profile could facilitate a more quantitative analysis, the multi-
level data with averaging kernels for 2020 are not publicly available, we therefore simply
averaged the observations for the corresponding altitudes. Consequently, the comparison
remains mainly qualitative.

4 Results

4.1 Parameter estimates

The $\lambda_{surface}$ was determined through laboratory Experiment No. 1. Based on Eq.10, the
parameter $\lambda_{surface}$ was estimated to be 0.0312 (uncertainty range: 0.0291 to 0.0317) for the 0.5
L air bags and 0.0255 (uncertainty range: 0.0250 to 0.0259) for the 4 L air bags (Fig. 3a, Table
1).

The isotopic fractionation coefficients α, were determined through laboratory Experiment
No. 2. From the averaged results of these measurements, using Eq.13, the water vapor isotopic
exchange coefficient, expressed as λ/α, was estimated to be 0.0249 for ^{18}O and 0.0244 for ^2H
(Fig. 3b and c). Consequently, $\alpha^{18}O$ was estimated to be 1.0241 (0.0255/0.0249), and α^2H was
estimated to be 1.0451 (0.0255/0.0244) (Fig. 3b and d). Two additional sets of fractionation
coefficients α, were obtained: $\alpha^{18}O = 1.0254$, $\alpha^2H = 1.0506$, and $\alpha^{18}O = 1.0264$, $\alpha^2H = 1.0380$
(Table 1).

The specific parameter values obtained in this study pertain to the Teflon air bags used in
the aforementioned tests, conducted at an ambient temperature of 16°C. These values depend
on bag material, temperature, and pressure, which should be considered when applying the
model under different conditions. We also noted batch-to-batch variations among air bags from
the same manufacturer. We apply α measured under ground-level storage and measurement
conditions, assuming negligible temperature and pressure effects during the short (10–20 min)
drone-based sampling period. Future work is needed to quantify these dependencies.
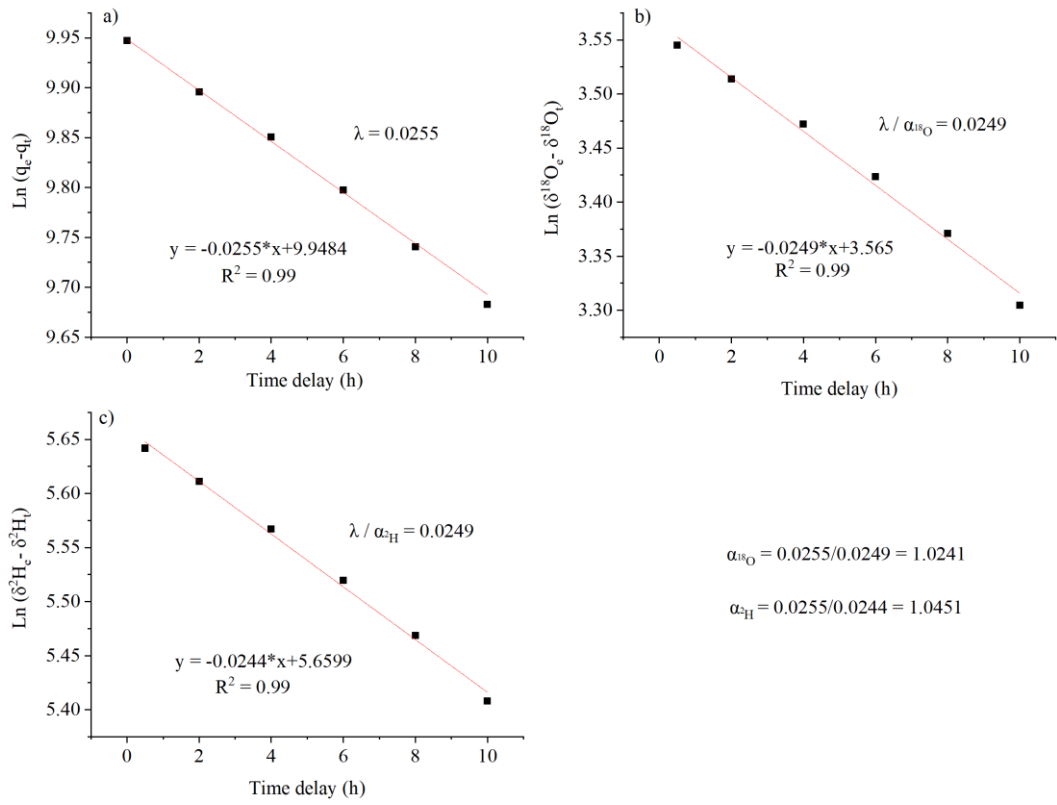
466

Figure 3 Determination of 3 parameters of the diffusion model : λ_{surface} (a) from Experiment No. 1, α¹⁸O (b), and α²H (c) from Experiment No. 2.

467 ## 4.2 **Diffusion model validation**

468 ### **4.2.1 General case**

469
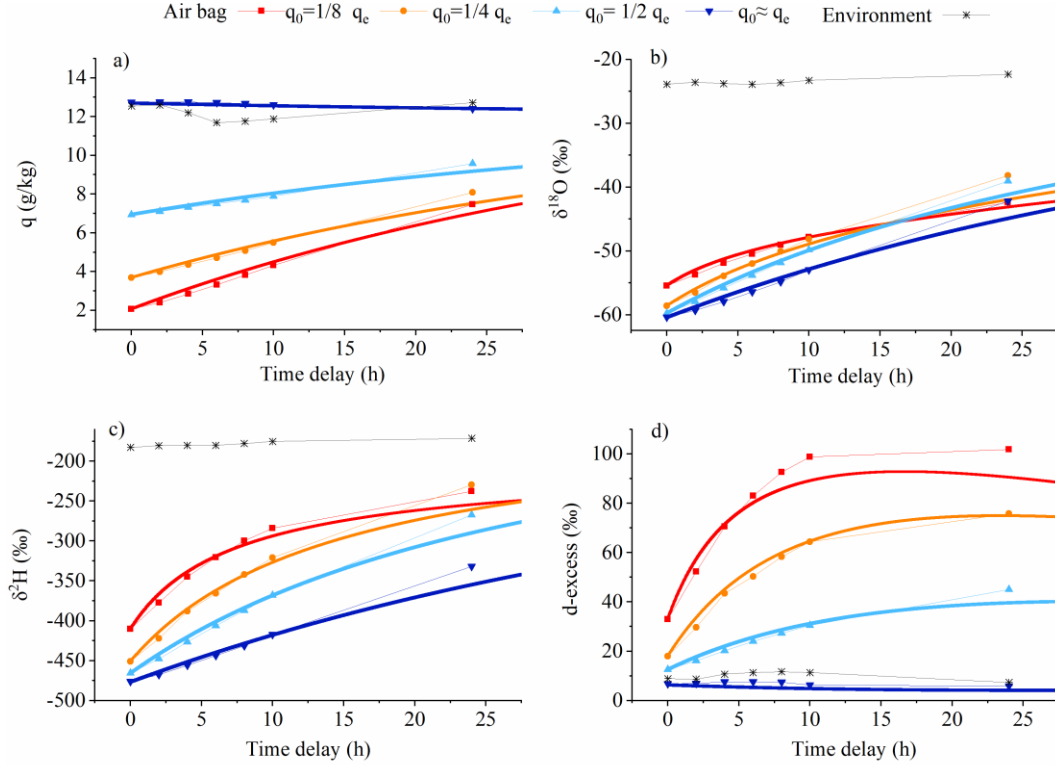
*Figure 4: Comparison of the variation within the air bag over time in laboratory permeability experiments (markers) and diffusion model simulations (lines) across a range of initial humidities at t = 0 (q$_0$), ranging from approximately 1/8 * q$_e$ to q$_e$ (q$_e$ denotes the environmental humidity), under the condition that the water vapor isotopic composition in the air bag significantly differs from ambient values : a) humidity; b) $\delta^{18}O$; c) δ^2H, d) d-excess.*

470   To validate the model, we used Experiment No.3 described in Subsection 3.2. The
471 diffusion model simulations (lines in Figs. 4, 5, 6, and Fig. A2) are in close agreement with our
472 experimental observations (markers in Figs. 4, 5, 6, and Fig. A2), showing consistency in
473 humidity, $\delta^{18}O$, δ^2H, and d-excess variations, with only minor deviations. Shorter storage times
474 produce fewer deviations. When the humidity inside the air bag is lower than the ambient level,
475 vapor from the environment enters the air bag, resulting in a gradual increase in humidity (Fig.
476 4a and Fig. A2). Meanwhile, because the water vapor isotopic composition in the air bag is
477 significantly lower than the ambient values, $\delta^{18}O$ and δ^2H in the air bag gradually increase and
478 toward ambient values as ambient moisture enters the bags over time (Fig. 4b and c). In contrast,
479 the d-excess increase as the time delay progresses due to kinetic fractionation during moisture
480 diffusion into the air bag (Fig. 4d), as detailed in the following Subsection 4.2.2.
481   We observed that some curves unexpectedly intersect, which can be understood by

482 analyzing Eq. 8. The first term $(\frac{\lambda}{\alpha} * (R_e - R_{(t)}))$ continuously drives $R_{(t)}$ towards R_e, while the

483   second term $(\frac{\lambda}{q_{(t)}}*(q_e-q_{(t)})*(\frac{R_e}{\alpha}-R_{(t)}))$ modulates the rate of change. Initially, for simulations

484   with lower q_0 (e.g., the red and orange curves), $q_e-q_{(t)}$ is large, making the second term

485   significant and positive, thereby increasing $R_{(t)}$ more rapidly. However, as $R_{(t)}$ exceeds R_e/α, the

486   sign of this term reverses, slowing down the increase in $R_{(t)}$ compared to other curves. In

487   contrast, curves with higher initial q_0 (e.g., blue curve) experience a steadier growth and

488   eventually surpass the initially faster-growing curves, leading to the observed crossing.

489   ### 4.2.2   Particular cases

490
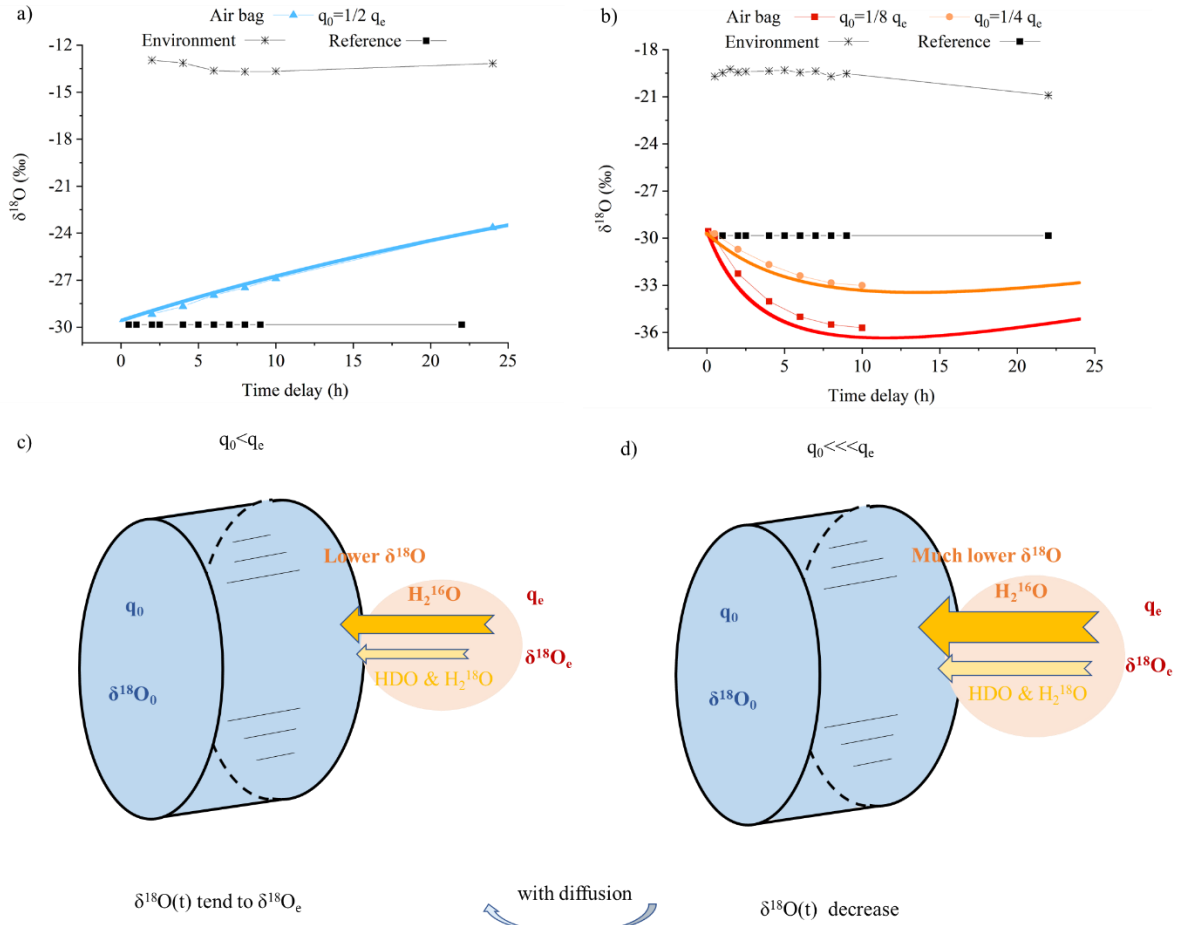
Figure 5   (a-b) Variations of $\delta^{18}O$ under different conditions: (a) when both the differences between internal ($\delta^{18}O_0$) and external ($\delta^{18}O_e$) $\delta^{18}O$ as well as between internal (q_0) and external (q_e) humidity are not significant, $\delta^{18}O$ gradually increases toward equilibrium; (b) when q_0 is significantly lower than q_e, a stronger vapor influx causes enhanced kinetic fractionation, leading to a decrease in $\delta^{18}O$. (c-d) Corresponding schematics: (c) illustrates the mechanism for (a), where a weaker humidity gradient results in slower isotopic shifts, while (d) corresponds to (b), showing intensified fractionation with a larger gradient, with arrows indicating vapor flux direction and fractionation intensity. $\delta^{18}O$ (t) is the variation of $\delta^{18}O$ within the air bag over time. In (a) and (b), the colored lines represent model simulations based on Eq.8, using parameterization from Experiments No. 1 and 2. Colored square markers show the corresponding experimental observations within the air bags. Black square markers

indicate the initial values inside the air bag, which remain constant over time and serve as a reference for comparison (legend: Reference).

491   Due to isotopic kinetic fractionation, lighter $H_2^{16}O$ molecules preferentially diffuse into
492 the air bag compared to heavier isotopologues such as $HD^{16}O$ and $H_2^{18}O$, resulting in a vapor
493 flux with lower $\delta^{18}O$ relative to ambient vapor (Fig. 2). Moreover, variations within the air bag
494 are driven by differences in water vapor content and isotopic ratios between its interior and
495 exterior, as described in the diffusion model in Section 2. As shown in the initial experiment
496 (Fig. 4b and c), when the internal $\delta^{18}O$ and $\delta^{2}H$ are significantly below the ambient values, the
497 δ-values of the diffusing vapor, although lower than ambient, still exceeds the initial internal δ-
498 values, leading to a gradual increase towards the ambient values; diffusion simply equilibrates
499 the isotopic composition in the bag and the environment. When the disparity between internal
500 and external $\delta^{18}O$ or $\delta^{2}H$ is not very substantial, and humidity differences are also minimal, the
501 weaker diffusive gradient produces less net kinetic fractionation. This results in a small amount
502 of vapor with lower $\delta^{18}O$ and $\delta^{2}H$ than the ambient moisture entering preferentially, but not
503 falling below internal initial values, thereby still drives a progressive increase in the internal
504 values towards ambient moisture (Fig. 5a and c). In contrast, with the same initial contrast
505 between internal and ambient δ-values, that is, the disparity between internal and external $\delta^{18}O$
506 and $\delta^{2}H$ is less pronounced, but q_0 is much lower than q_e, there is a stronger net flux into the
507 bag, and this flux fractionates more rapidly; much more vapor with significantly lower $\delta^{18}O$
508 and $\delta^{2}H$ than the ambient moisture (and lower values than the initial internal vapor) enters the
509 air bags and dominates their isotopic composition, thereby reducing the internal δ-values (Fig.5
510 b and d). The smaller the difference in humidity and isotopic composition between the inside
511 and outside of the air bag, the slower and smaller the isotopic change in the vapor within the
512 air bag (Fig. 5 and Fig. 6).

513

514
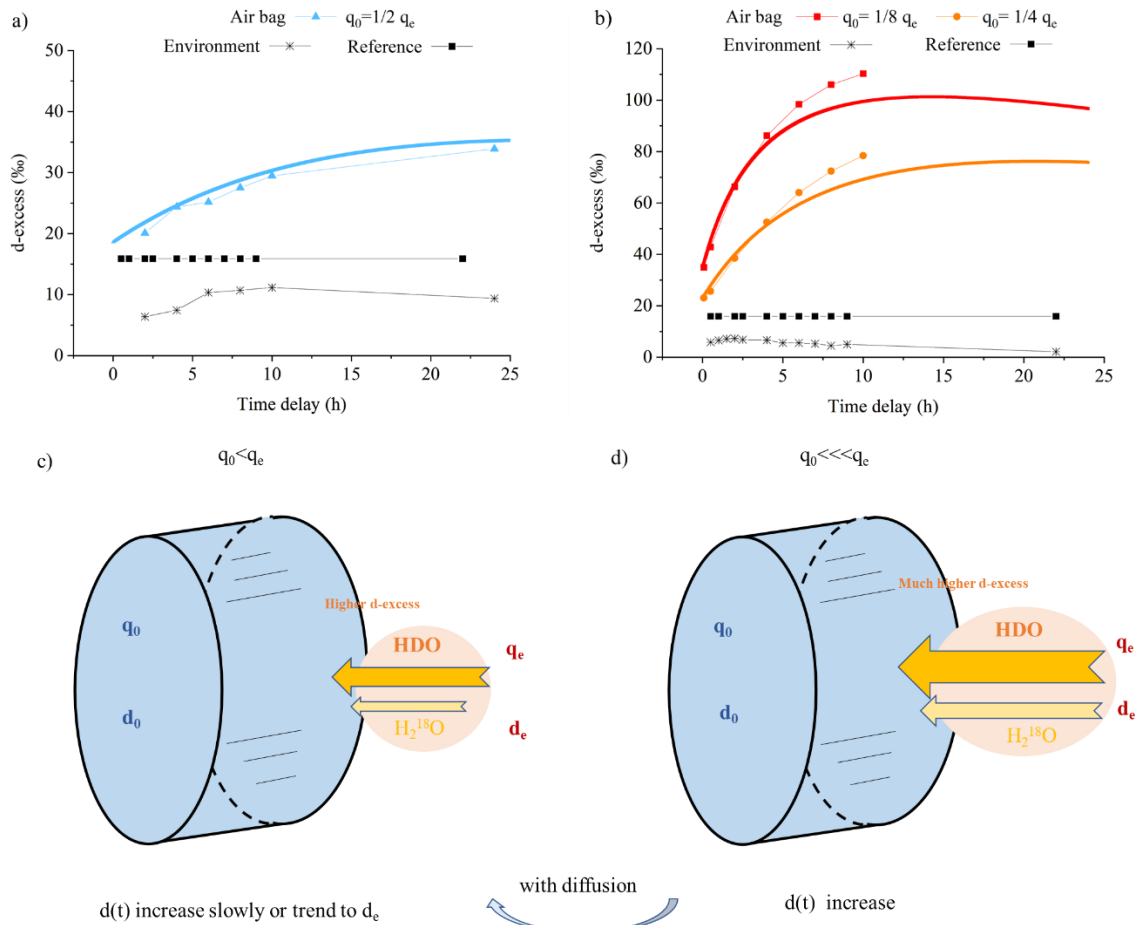
Figure 6 (a-b) Same as Fig.5, but showing the evolution of d-excess: (a) when the difference between the humidity inside (q_0) and outside (q_e) the air bag is not significant, d-excess increases gradually; (b) when q_0 is significantly lower than q_e, a stronger vapor influx enhances kinetic fractionation, causing a more rapid d-excess increase. (c-d) Corresponding schematics: (c) illustrates the mechanism for (a), where a smaller humidity gradient results in slower isotopic shifts, while (d) corresponds to (b), showing intensified fractionation with a larger gradient. d_0 indicates the initial d-excess at $t = 0$, d_e represents the d-excess in the environment. $d(t)$ denotes the variation of d-excess within the air bag over time.

In addition, because HDO and $H_2^{18}O$ diffuse at similar rates the magnitude of the kinetic fractionation for D and ^{18}O is similar. However, since d-excess reflects deviations relative to the 8:1 fractionation ratio typical of equilibrium processes, the tendency is for kinetic fractionation during diffusion to contribute vapor with high d-excess and cause an increase in d-excess during air bag storage as water vapor is added to the bag (Fig. 6a and c). When the humidity difference between the inside and outside of the air bag increases, the d-excess of the incoming vapor flux increases as a result of more intensive kinetic fractionation. This leads to a faster increase in the vapor d-excess inside the air bag (Fig. 6b and d).

Regardless of the differences in water vapor humidity and isotopic compositions inside and outside the air bag, the diffusion model simulations closely match the experimental observations (Figs.4, 5 and 6). Using the method described in Subsection 3.4.2, the average difference between all simulations and experimental data for each parameter represented the

535   model-experiment mismatch: 0.5 ‰ for δ¹⁸O, 4.1 ‰ for δ²H, and 2.9 ‰ for d-excess.

536   4.3 **Raw and corrected vertical profiles**

537   Here, we present a summary of drone-based observations from the field campaign at Mount
538 Laojun, Lijiang, on the southeastern edge of the Tibetan Plateau and the northwestern of the
539 Yunnan-Guizhou Plateau, China, conducted between June 25, 2020, and October 17, 2020.

540
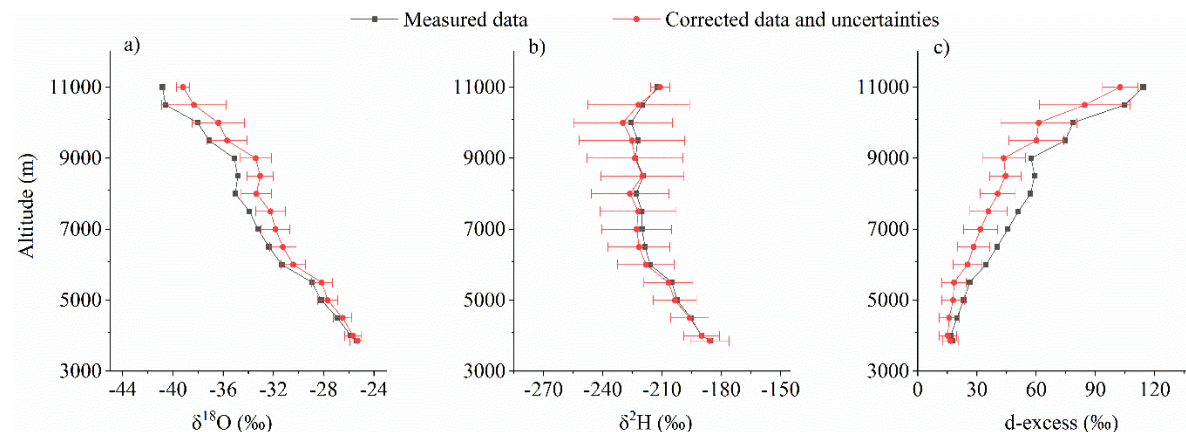
Figure 7 Comparison of vertical profiles for the mean values of all raw measurements and corrected data from June to October, and associated uncertainties for δ¹⁸O (a), δ²H (b) and d-excess (c).

541   As altitude increases, vapor δ¹⁸O and δ²H decrease due to condensation and precipitation
542 processes that occur as air masses ascend, which preferentially remove heavier isotopes
543 following Rayleigh distillation (Dansgaard, 1964). Meanwhile, the d-excess rises. This pattern
544 aligns with previous observations in the lower troposphere (He and Smith, 1999; Salmon et al.,
545 2019) and simulations of complete vertical profiles (Bony et al., 2008).
546   In our observations, the variation in δ¹⁸O across the vertical profile from ground level at
547 3856 meters to 11 km is approximately 10-15‰. However, as altitude increases, the air becomes
548 progressively drier, leading to a greater disparity in humidity between the air collected in the
549 air bag and the surface storage environment. This aligns with the variations in Subsection 4.2.2
550 (Figs. 5b, 5d, and 6b, 6d). The strong kinetic fractionation driven by the diffusion of air into the
551 air bag results in a decrease in the water vapor δ¹⁸O within the bag. After applying model
552 corrections, the corrected δ¹⁸O inside the bag increased slightly compared to pre-correction
553 levels. As described in Subsection 4.2, vapor flux with higher d-excess entering the bag
554 increases the d-excess inside. As a compensation, the diffusion model applies corrections,
555 resulting in a reduced d-excess after correction (Fig. 7c and 10).

556   4.4 **Uncertainty estimates**

557   According to the method of uncertainty estimation elaborated in Subsection 3.4.2, we
558 investigated four error sources to evaluate uncertainty (Table 1).
559
560
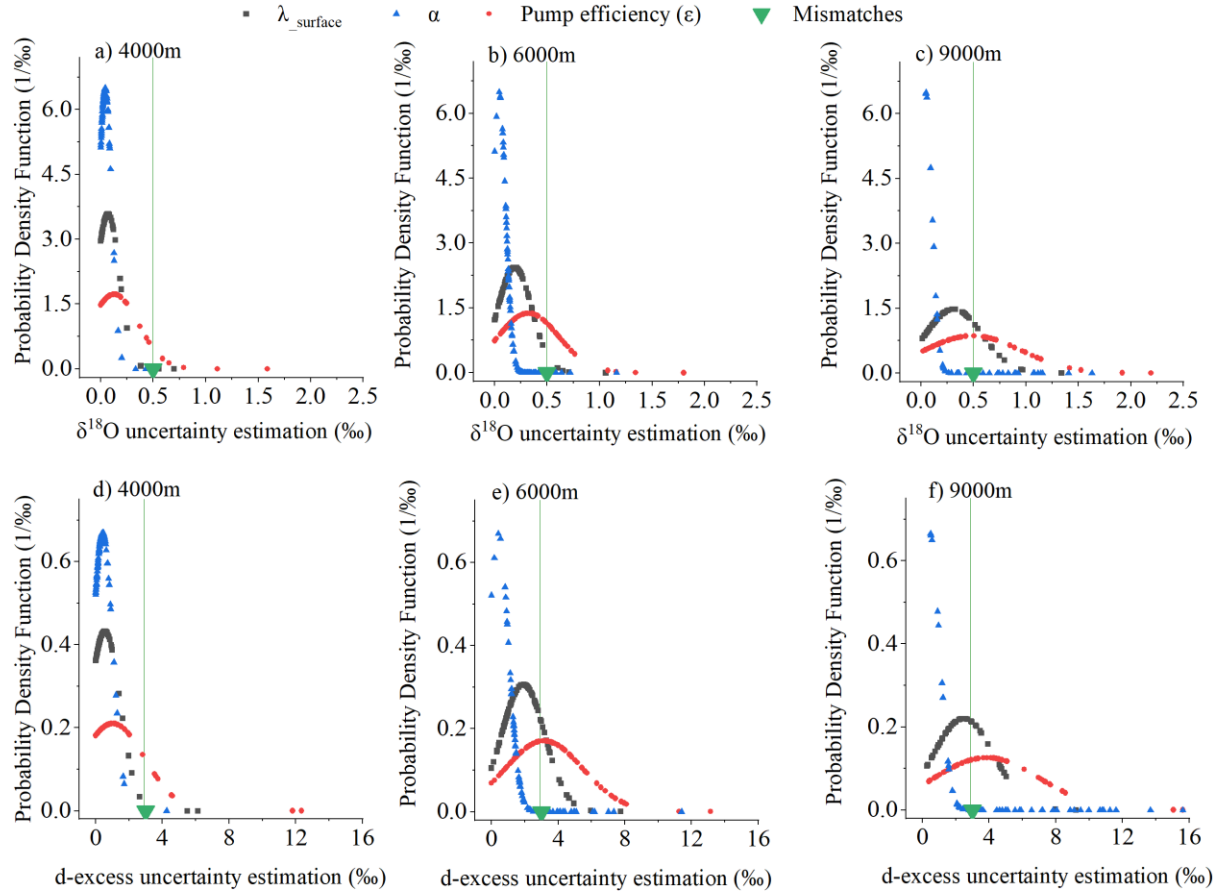
Figure 8: Contributions of different sources of uncertainty for $\delta^{18}O$ (a, b, c for 4000m, 6000m, 9000m, respectively) and d-excess (d, e, f for 4000m, 6000m, 9000m, respectively). The green triangle shows the average mismatch between the model and experimental results. The peak position of each probability density function (PDF) represents the most likely uncertainty value for a given source, while the width of the distribution reflects the variability.

We represent the contribution of each source of uncertainty to vertical vapor $\delta^{18}O$ and d-excess measurements at different altitudes using probability density function plots (Fig. 8). Each PDF peak indicates the most probable uncertainty value, while its width reflects sensitivity to that parameter. Narrow PDFs suggest stable, well-constrained uncertainty sources, whereas broader PDFs indicate greater variability and a more diffuse impact on the correction outcome. The mismatch between the model and the experiment (green marker), calculated using the method described in Subsection 3.4.2, is assumed to remain constant across all altitudes. The other three error sources manifest as unimodal normal distributions at various altitudes for both $\delta^{18}O$ and d-excess. Errors due to uncertainties in pump efficiency (ε) are the main source, exhibiting the largest spread (Fig. 8) and increasing with altitude (Fig. 9). Errors derived from $\lambda_{surface}$ and α also increase with altitude (Figs. 8 and 9). As a result, at higher elevations, the satellite δ^2H differs more from the measured and corrected data than at lower altitudes (Fig. 10). This pattern arises because λ_{alt} deviates more from $\lambda_{surface}$ at higher elevations (Eq.16), primarily due to increased errors in estimating M_{alt}, amplifying correction errors. Moreover, the humidity and isotopic disparity between the air captured in the air bag and lower-altitude ambient air widens with altitude, requiring more intensive corrections. Consequently,

578 both the uncertainty (Figs. 8 and 9) and the magnitude of the diffusion correction (Fig. 7)
579 increase with altitude.

580
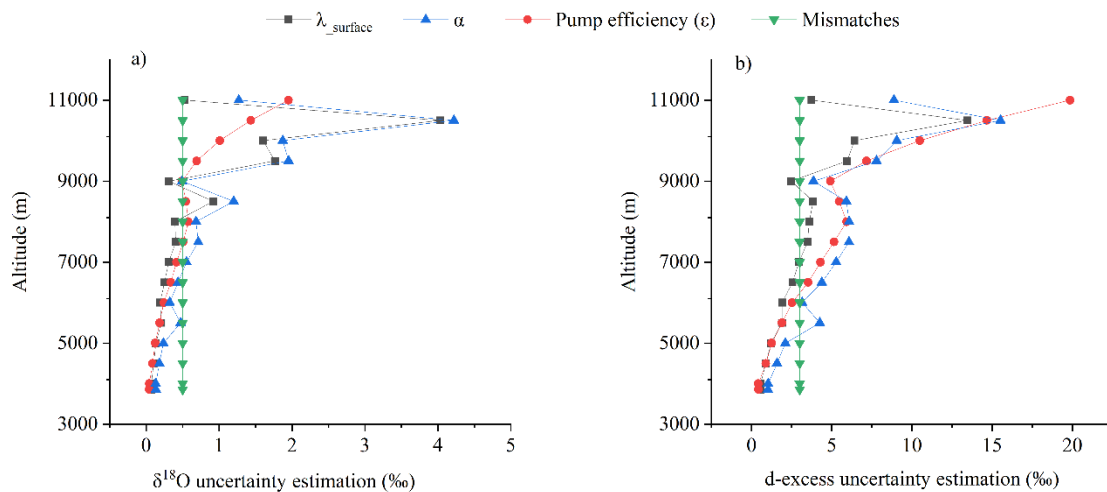
Figure 9 Mean uncertainty of $\delta^{18}O$ (a) and d-excess (b) with altitude for different sources.

581 On the contrary, errors pertaining to $\lambda_{surface}$ and α diminish at altitudes exceeding 10,500
582 meters. This phenomenon may be attributed to our sampling methodology. Although we
583 collected air samples in sequence from low to high altitudes, these samples were measured in
584 reverse order, from high to low altitudes. Consequently, samples taken from the highest
585 altitudes had the shortest storage durations, typically ranging from 10 minutes to two hours.
586 Additionally, we extended the sampling times with increasing altitude (Fig. A1). These
587 extended sampling periods and reduced storage durations help to partially offset the amplified
588 disparities observed between the raw and corrected profiles at higher altitudes. During the
589 drone-based sampling period, which lasted around 10-20 minutes, the external conditions
590 impacting the air bags were not the ground-level environmental values used in the model but
591 rather those of the vertical profile. However, the humidity at higher altitudes is lower than at
592 ground level, and the isotopic composition are closer to those inside the airbag. Consequently,
593 its impact on the airbag's internal conditions is less significant than suggested by using ground-
594 level environmental values. Therefore, the overestimated error in our model accounted for these
595 potential discrepancies.

596 The combined uncertainty from all sources, including $\lambda_{surface}$, α, pump efficiency (ε), and
597 model-experiment mismatches, result in a total uncertainty of approximately 1‰ for $\delta^{18}O$ and
598 8‰ for d-excess across 98% of the data. The corresponding 95% confidence intervals are
599 approximately 0.9‰ for $\delta^{18}O$ and 6.9‰ for d-excess. This range is acceptable when compared
600 to the substantial vertical variations we observed (~20‰ for $\delta^{18}O$ and ~100 ‰ for d-excess).
601 Among these sources, ε contributes the largest uncertainty, particularly at higher altitudes (Fig.
602 8), likely due to the conservative uncertainty range we applied to account for potential
603 reductions in collected air mass at high altitudes. Additionally, $\lambda_{surface}$ and α also contributes
604 considerably to the total uncertainty (Figs. 8 and 9). To mitigate this, we recommend conducting
605 multiple measurements to obtain an averaged value and performing repeated parameter
606 validation to ensure robustness.

4.5 **Comparison with Picarro measurements and satellite data**

608
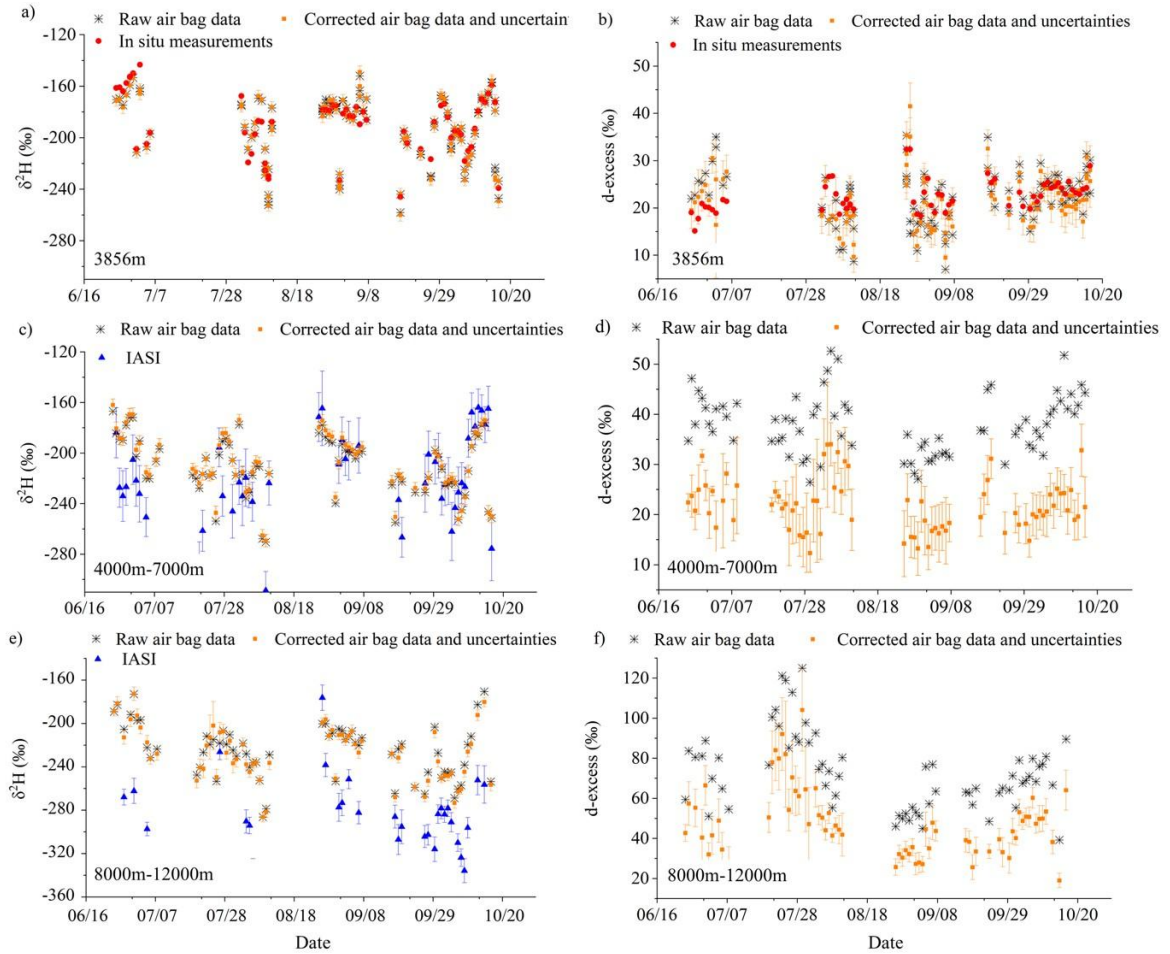
Figure 10 Time series comparison for δ²H (a, c, e) and d-excess (b, d, f):

(a, b) Raw and corrected (with uncertainties) instantaneous air bag measurements at the surface (3856 m), compared with Picarro in-situ measurements at the same altitude, averaged over the sampling period.

(c, d) Raw and corrected (with uncertainties) altitude-averaged air bag measurements from 4000 m to 7000 m, compared with satellite data (IASI), which also include uncertainty ranges accounting only for retrieval-fit noise and the atmospheric temperature a priori constraint.

(e, f) Raw and corrected (with uncertainties) altitude-averaged air bag measurements from 8000 m to 12000 m, compared with satellite data (IASI).

609   The left panel of Fig.10 (Figs. 10 a, c, and e) shows the comparison of raw and corrected
610 water vapor δ^2H measurements at different altitudes with in-situ surface-level measurements
611 on the Picarro or IASI satellite data at corresponding altitudes.
612   At near-ground level, both the raw and corrected δ^2H and d-excess values from the bag
613 measurements show close agreement with the in-situ Picarro observations (Fig. 10a and b),
614 indicating minimal diffusion effects under nearly identical humidity and isotopic conditions

between the inside and outside of the bags. Most data points are distributed along the 1:1 line (Fig. A3), while d-excess shows slightly larger scatter. After applying the correction, the agreement improved: the correlation coefficient between the bag and Picarro δ^2H values increased from 0.90 to 0.99, and for d-excess from 0.41 to 0.72. The mean absolute error (MAE) between the corrected bag and Picarro measurements is 3.0‰ for δ^2H and 1.4‰ for d-excess. These discrepancies are within the uncertainty range derived from laboratory diffusion experiments and model–experiment mismatches, which were comprehensively incorporated in the error estimation (Sections 3.2 and 3.4): 0.5 ‰ for $\delta^{18}O$, 4.1 ‰ for δ^2H, and 2.9 ‰ for d-excess. The differences also can be attributed to the fact that the Picarro in-situ observations are period-averaged, whereas the bag samples represent instantaneous values.

To compare corrected measurements with observations at higher altitudes, we refer to the IASI satellite dataset. We acknowledge that this comparison is qualitative, as satellite data represent vertical averages over layers defined by averaging kernels, and therefore differ in measurement footprints (both horizontal and vertical) and spatio-temporal sampling disparities (Shi et al., 2020). A more quantitative analysis could be facilitated if an averaging kernel is used to smooth the observed profiles (Herman et al., 2014), but even after such adjustment, substantial differences would likely persist. IASI provides only two overpasses per day (around 09:30 LT AM and PM), whereas our drone-based measurements were conducted locally during daytime. The IASI footprint (~12 km at nadir) provides coarse spatial averaging, whereas our measurements are local and instantaneous, limiting its ability to capture fine-scale variability at the sampling site. Importantly, IASI cannot observe through or below thick clouds such as anvils, and thus mainly samples air outside convective detrainment regions. Because convective detrainment isotopically enriches vapor (Kuang et al., 2003; Moyer et al., 1996; Smith et al., 2006; Vries et al., 2021; Webster and Heymsfield, 2003), the air masses observed by IASI— being farther from detrainment—are expected to be more depleted. This cloud-sampling limitation may therefore contribute to the lower δ^2H values retrieved by IASI in the upper troposphere compared with our in-situ observations. Such fundamental mismatches in vertical weighting, temporal coverage, and spatial representativeness are noted in previous satellite–in-situ intercomparisons, which found that satellites capture large-scale isotopic gradients but smooth out fine-scale vertical and diurnal variations (Herman et al., 2014; Lacour et al., 2018). These complementary characteristics highlight the value of combining satellite and high-resolution in-situ observations: satellites provide synoptic coverage, while local observations resolve small-scale processes that shape the isotopic structure of the atmosphere. Overall, our comparison with IASI should thus be regarded as a qualitative consistency check confirming large-scale and temporal coherence rather than a one-to-one correspondence.

For most intervals, IASI satellite data closely match raw and corrected δ^2H measurements for altitudes 4000–7000m. In the 8000–12000m range, although applying the diffusion correction increased the correlation coefficient between the air-bag observations and the IASI data from 0.53 to 0.60, IASI data are lower than δ^2H air-bag observations during certain periods, particularly June and September 2020; one possible reason is unaccounted environmental influences at high altitudes. However, it is noteworthy that the IASI data closely match the observed δ^2H for all other periods in the 4000–7000 m range, except for June 2020, where they are lower too. Moreover, diffusion within the sampling bags could, in principle, introduce systematic bias, yet the IASI values sometimes agree well, sometimes appear higher, and

sometimes lower than our measurements (Fig. 10). Therefore, the differences between our in-situ observations and the IASI retrievals likely arise mainly from representativeness differences intrinsic to the satellite data, as discussed above—practically the cloud-sampling limitation in the upper troposphere—rather than from diffusion-related biases. Accordingly, such variations cannot be corrected by the diffusion model, which accounts for isotopic fractionation during air-bag storage but not for spatiotemporal or cloud-sampling discrepancies between observation platforms.

The right panel of Fig.10 (Figs. 10 b, d, and f) shows the comparison of raw and corrected vapor d-excess measurements. No d-excess dataset is available for comparison for the 4000–7000m and 8000–12000m (Fig. 10d and f). As previously noted, corrected d-excess values should be and are lower than the raw data, as expected from diffusion theory. For the 8000–12000 m observations, the correction magnitude is relatively smaller than at lower altitudes due to the shorter storage time of the air bags.

Although no completely independent dataset is available for direct validation, our model—already verified by laboratory experiments—was used to perform a detailed assessment of all potential error sources and to quantify a comprehensive and conservative uncertainty range of the corrected data.

5   Conclusion

High spatial and temporal resolution water vapor isotope data are critical for understanding various hydrologic cycle processes. However, observations of vertical water vapor isotope profiles are scarce, particularly in the upper troposphere. Satellite-derived vapor isotope data are available only at limited vertical and temporal resolutions. Acquiring high-resolution water vapor isotope data, especially under conditions where direct measurements are difficult, has been a significant challenge for the water isotopes research community. This study demonstrates the potential of a drone-based air bag sampling method to overcome this challenge, offers solutions for evaluating air bag suitability and addressing air bag permeability.

While air bags offer the advantage of sample collection, their inherent permeability can affect the sealing integrity of the samples, leading to potential contamination. The permeability of airbag materials varies, with some exhibiting lower levels. We recommend prioritizing the use of glass containers and air bags with the lowest permeability for collecting water vapor using portable devices. Additionally, it is essential to conduct the permeability experiments described in this article before any experimental undertaking. This involves storing water vapor with known isotopic composition in the portable collection device for an extended period and then re-measuring these values to assess or determine the device's permeability parameters.

To further address the permeability challenge, we developed a mathematical model to evaluate and correct for diffusion and isotopic fractionation, ensuring the reliability of vapor isotope measurements using air bags. Calibrated with parameters from laboratory experiments, our correction model reconstructs the initial isotopic composition of sampled vapor by using data from both the air bag and the surrounding environment, offers a potential solution to the prevalent permeability challenges. This model was rigorously validated against observational experiments conducted under varying conditions. We also applied this model to drone-collected

samples at various pressures. By estimating uncertainty and comparing corrected data with in-situ surface-level measurements on the Picarro and satellite observations, we validated the reliability and applicability of drone-based water vapor isotope measurements.

Our drone-based sampling system, combined with the diffusion model, effectively addresses the limitations of traditional high-altitude water vapor measurement methods. It meets the need for lightweight equipment while providing a more economical, efficient, and flexible alternative to conventional approaches involving large aircraft, airships, and balloons. This approach enables us to exploit the benefits of drone-based air bag sampling at high altitudes and over long distances, while effectively mitigating its potential limitations. This strategy significantly broadens its potential applications across various environments, thereby enhancing the range and richness of data that can be gathered for water vapor isotope research.

This study was conducted under stable temperature and equal internal and external pressures during storage. We acknowledge that a formulation based on partial pressure of water vapor would be more general and could improve model applicability under varying temperature and pressure conditions. Future work could extend the model to account for these factors.

Code availability

The diffusion modeling code, which simulates the evolution of water vapor isotopes in the airbag and corrects them to their initial values, is available at:

https://github.com/DishiWANG0608/Correcting-for-water-vapor-diffusion.git

Data availability

Data are available from the authors on request.

Video supplement

A video showcasing our field campaign on drone-derived water vapor isotope sampling up to the upper troposphere (11 km) during convective activity, including the workflow for airbag water vapor isotope sampling, is currently available upon request and will be publicly accessible in the near future. Please contact the corresponding author for access (di.wang@latmos.ipsl.fr).

Author contributions

D.W., C.R., and L.T. designed the research, established the subjects of the methodology, and performed the analysis; D.W. and D.Y. conducted the observations; G.B., S.F., H.P. and L.L. contributed to the establishment of methodologies, data calibration, and analysis; Y.S. provided assistance with the computing; All authors contributed to the discussion of the results

732 and the final article; D.W. drafted the manuscript with contributions from all co-authors.

Competing interests

734 The contact author has declared that none of the authors has any competing interests.

Acknowledgments

736 The authors gratefully acknowledge the Infrared Atmospheric Sounding Interferometer
737 (IASI) for providing spatiotemporal coverage of δ^2H retrieval. We thank Jiaping Xu, Mingjian
738 Chen, Le Chan, and Yao Yao for their irreplaceable help in the development of the drones. We
739 are grateful to the management of 99 Dragon, Mountain Laojun in Lijiang for facilitating the
740 field experiments. We thank Pengbin Liang and Jiangrong Tai for partially participating in the
741 field observations. We acknowledge Hans Christian Steen-Larsen and Harald Sodemann for
742 their discussions on the correction method. We acknowledge the use of OpenAI's ChatGPT to
743 assist in refining the language. This work was supported by the National Natural Science
744 Foundation of China (Grants No. 42401043 and U2202208), the fellowship from the China
745 Postdoctoral Science Foundation (Grant No.2025T180092), the Strategic Priority Research
746 Program of the Chinese Academy of Sciences (Grant No. XDB40000000), and the Science and
747 Technology Department of Yunnan Province (Grant No. 202201BF070001-021). Di Wang
748 acknowledges support from Chinese Scholarship Council and the Postdoctoral Fellowship
749 Program of China Postdoctoral Science Foundation (Grant No. GZC20241440). Siteng Fan
750 acknowledges support from the Marie Skłodowska-Curie Actions of European Research
751 Executive Agency (Grant No. 101064814) and the High Level Special Fund of Southern
752 University of Science and Technology (Grant No. G03050K001).

References

754 Ayliffe, L., Cerling, T., Robinson, T., West, A., Sponheimer, M., Passey, B., Hammer, J., Roeder, B.,
755 Dearing, M., Ehleringer, J., 2004. Turnover of carbon isotopes in tail hair and breath CO_2 of horses fed
756 an isotopically varied diet. Oecologia 139, 11-22.
757 Bony, S., Risi, C., Vimeux, F., 2008. Influence of convective processes on the isotopic composition
758 ($\delta18O$ and δD) of precipitation and water vapor in the tropics: 1. Radiative-convective equilibrium and
759 Tropical Ocean–Global Atmosphere–Coupled Ocean-Atmosphere Response Experiment (TOGA-COARE)
760 simulations. Journal of Geophysical Research: Atmospheres 113.
761 Bowen, G.J., Cai, Z., Fiorella, R.P., Putman, A.L., 2019. Isotopes in the Water Cycle: Regional-to
762 Global-Scale Patterns and Applications. Annual Review of Earth and Planetary Sciences 47.
763 Brienen, R.J., Schöngart, J., Zuidema, P.A., 2016. Tree rings in the tropics: insights into the ecology
764 and climate sensitivity of tropical trees. Tropical tree physiology: adaptations and responses in a
765 changing environment, 439-461.
766 Cerling, T.E., Wittemyer, G., Rasmussen, H.B., Vollrath, F., Cerling, C.E., Robinson, T.J., Douglas-

767 Hamilton, I., 2006. Stable isotopes in elephant hair document migration patterns and diet changes.
768 Proceedings of the National Academy of Sciences 103, 371-373.

769 Dansgaard, W., 1964. Stable isotopes in precipitation. Tellus 16, 436-468.

770 Diekmann, C.J., Schneider, M., Ertl, B., Hase, F., García, O., Khosrawi, F., Sepúlveda, E., Knippertz, P.,
771 Braesicke, P., 2021. The global and multi-annual MUSICA IASI {H 2 O, δ D} pair dataset. Earth System
772 Science Data 13, 5273-5292.

773 Fick, A., 1855. Ueber diffusion. Annalen der physik 170, 59-86.

774 Galewsky, J., Steen-Larsen, H.C., Field, R.D., Worden, J., Risi, C., Schneider, M., 2016. Stable isotopes
775 in atmospheric water vapor and applications to the hydrologic cycle. Reviews of Geophysics 54.

776 Gat, J.R., 1996. Oxygen and hydrogen isotopes in the hydrologic cycle. Annual Review of Earth and
777 Planetary Sciences 24, 225-262.

778 Ghosh, P., Brand, W.A., 2003. Stable isotope ratio mass spectrometry in global climate change
779 research. International Journal of Mass Spectrometry 228, 1-33.

780 Gralher, B., Herbstritt, B., Weiler, M., 2021. Unresolved aspects of the direct vapor equilibration
781 method for stable isotope analysis (δ 18 O, δ 2 H) of matrix-bound water: unifying protocols through
782 empirical and mathematical scrutiny. Hydrology and Earth System Sciences 25, 5219-5235.

783 Grootes, P.M., Stuiver, M., 1997. Oxygen 18/16 variability in Greenland snow and ice with 10(-3)-
784 to 10(5)-year time resolution. Journal of Geophysical Research-Oceans 102, 26455-26470.

785 Havranek, R.E., Snell, K.E., Davidheiser-Kroll, B., Bowen, G.J., Vaughn, B., 2020. The Soil Water
786 Isotope Storage System (SWISS): An integrated soil water vapor sampling and multiport storage system
787 for stable isotope geochemistry. Rapid Communications in Mass Spectrometry 34, e8783.

788 He, H., Smith, R.B., 1999. Stable isotope composition of water vapor in the atmospheric boundary
789 layer above the forests of New England. Journal of Geophysical Research Atmospheres 104, 11657-
790 11673.

791 Hendry, M., Schmeling, E., Wassenaar, L., Barbour, S., Pratt, D., 2015. Determining the stable
792 isotope composition of pore water from saturated and unsaturated zone core: improvements to the
793 direct vapour equilibration laser spectrometry method. Hydrology and Earth System Sciences 19, 4427-
794 4440.

795 Herbstritt, B., Gralher, B., Seeger, S., Rinderer, M., Weiler, M., 2023. Discrete in situ vapor sampling
796 for subsequent lab-based water stable isotope analysis. Hydrology and Earth System Sciences 27, 3701-
797 3718.

798 Herman, R., Cherry, J., Young, J., Welker, J., Noone, D., Kulawik, S., Worden, J., 2014. Aircraft
799 validation of Aura Tropospheric Emission Spectrometer retrievals of HDO/H 2 O. Atmospheric
800 Measurement Techniques 7, 3127-3138.

801 Hodges, J.T., Lisak, D., 2006. Frequency-stabilized cavity ring-down spectrometer for high-
802 sensitivity measurements of water vapor concentration. Applied Physics B 85, 375-382.

803 JingfengLiu,   CundeXiao,   MinghuDing,   JiawenRen,   2014.
804 Variationsinstablehydrogenandoxygenisotopesinatmosphericwatervaporinthemarineboundarylayeracr
805 ossawidelatituderange. Journal of Environmental Sciences 26, 2266-2276.

806 Johnson, L., Sharp, Z., Galewsky, J., Strong, M., Van Pelt, A., Dong, F., Noone, D., 2011. Hydrogen
807 isotope correction for laser instrument measurement bias at low water vapor concentration using
808 conventional isotope analyses: application to measurements from Mauna Loa Observatory, Hawaii.
809 Rapid Communications in Mass Spectrometry 25, 608-616.

810 Kuang, Z., Toon, G.C., Wennberg, P.O., Yung, Y.L., 2003. Measured HDO/H2O ratios across the

811 tropical tropopause. Geophysical Research Letters 30.

812 Lacour, J.-L., Risi, C., Worden, J., Clerbaux, C., Coheur, P.-F., 2018. Importance of depth and intensity
813 of convection on the isotopic composition of water vapor as seen from IASI and TES δD observations.
814 Earth and planetary science letters 481, 387-394.

815 Magh, R.-K., Gralher, B., Herbstritt, B., Kübert, A., Lim, H., Lundmark, T., Marshall, J., 2022.
816 Conservative storage of water vapour–practical in situ sampling of stable isotopes in tree stems.
817 Hydrology and Earth System Sciences 26, 3573-3587.

818 Michener, R., Lajtha, K., 2008. Stable isotopes in ecology and environmental science. John Wiley &
819 Sons.

820 Millar, C., Pratt, D., Schneider, D.J., McDonnell, J.J., 2018. A comparison of extraction systems for
821 plant water stable isotope analysis. Rapid Communications in Mass Spectrometry 32, 1031-1044.

822 Moyer, E.J., Irion, F.W., Yung, Y.L., Gunson, M.R., 1996. ATMOS stratospheric deuterated water and
823 implications for troposphere-stratosphere transport. Geophysical Research Letters 23, 2385-2388.

824 Muccio, Z., Jackson, G.P., 2009. Isotope ratio mass spectrometry. Analyst 134, 213-222.

825 Rodgers, C.D., Connor, B.J., 2003. Intercomparison of remote sounding instruments. Journal of
826 Geophysical Research: Atmospheres 108.

827 Rozmiarek, K.S., Vaughn, B.H., Jones, T.R., Morris, V., Skorski, W.B., Hughes, A.G., Elston, J., Wahl,
828 S., Faber, A.-K., Steen-Larsen, H.C., 2021. An unmanned aerial vehicle sampling platform for atmospheric
829 water vapor isotopes in polar environments. Atmospheric Measurement Techniques 14, 7045-7067.

830 Salmon, O.E., Welp, L.R., Baldwin, M.E., Hajny, K.D., Stirm, B.H., Shepson, P.B., 2019. Vertical profile
831 observations of water vapor deuterium excess in the lower troposphere. Atmospheric Chemistry and
832 Physics 19, 11525-11543.

833 Schmidt, M., Maseyk, K., Lett, C., Biron, P., Richard, P., Bariac, T., Seibt, U., 2010. Concentration
834 effects on laser-based δ18O and δ2H measurements and implications for the calibration of vapour
835 measurements with liquid standards. Rapid Communications in Mass Spectrometry 24, 3553-3561.

836 Schneider, A., Borsdorff, T., Aemisegger, F., Feist, D.G., Kivi, R., Hase, F., Schneider, M., Landgraf, J.,
837 2020. First data set of H 2 O/HDO columns from the Tropospheric Monitoring Instrument (TROPOMI).
838 Atmospheric Measurement Techniques 13, 85-100.

839 Shi, X., Risi, C., Pu, T., Lacour, J.l., Kong, Y., Wang, K., He, Y., Xia, D., 2020. Variability of isotope
840 composition of precipitation in the southeastern Tibetan Plateau from the synoptic to seasonal time
841 scale. Journal of Geophysical Research: Atmospheres 125, e2019JD031751.

842 Smith, J.A., Ackerman, A.S., Jensen, E.J., Toon, O.B., 2006. Role of deep convection in establishing
843 the isotopic composition of water vapor in the tropical transition layer. Geophysical Research Letters 33,
844 0_46-40_47.

845 Sprenger, M., Herbstritt, B., Weiler, M., 2015. Established methods and new opportunities for pore
846 water stable isotope analysis. Hydrological Processes 29, 5174-5192.

847 Steen-Larsen, H.C., Masson-Delmotte, V., Sjolte, J., Johnsen, S.J., Vinther, B.M., Bréon, F.M.,
848 Clausen, H.B., Dahl-Jensen, D., Falourd, S., Fettweis, X., 2011. Understanding the climatic signal in the
849 water stable isotope records from the NEEM shallow firn/ice cores in northwest Greenland. Journal of
850 Geophysical Research Atmospheres 116, 161-165.

851 Vries, A.D., Aemisegger, F., Pfahl, S., Wernli, H., 2021. Stable water isotope signals in tropical ice
852 clouds in the West African monsoon simulated with a regional convection-permitting model.

853 Wassenaar, L., Hendry, M., Chostner, V., Lis, G., 2008. High resolution pore water δ2H and δ18O
854 measurements by H2O (liquid)– H2O (vapor) equilibration laser spectroscopy. Environmental science &

855 technology 42, 9262-9267.

856 Webster, C.R., Heymsfield, A.J., 2003. Water isotope ratios D/H, O-18/O-16, O-17/O-16 in and out
857 of clouds map dehydration pathways. Science 302, 1742-1745.

858 West, A.G., Goldsmith, G.R., Brooks, P.D., Dawson, T.E., 2010. Discrepancies between isotope ratio
859 infrared spectroscopy and isotope ratio mass spectrometry for the stable isotope analysis of plant and
860 soil waters. Rapid Communications in Mass Spectrometry 24, 1948-1954.

861 West, J.B., Bowen, G.J., Dawson, T.E., Tu, K.P., 2009. Isoscapes: understanding movement, pattern,
862 and process on Earth through isotope mapping. Springer.

863 Worden, J., Bowman, K., Noone, D., Beer, R., Clough, S., Eldering, A., Fisher, B., Goldman, A.,
864 Gunson, M., Herman, R., Kulawik, S.S., Lampel, M., Luo, M., Osterman, G., Rinsland, C., Rodgers, C.,
865 Sander, S., Shephard, M., Worden, H., 2006. Tropospheric emission spectrometer observations of the
866 tropospheric HDO/H2O ratio: Estimation approach and characterization. Journal of Geophysical
867 Research-Atmospheres 111.

868 Worden, J.R., Kulawik, S.S., Fu, D., Payne, V.H., Bowman, K.W., 2019. Characterization and
869 evaluation of AIRS-based estimates of the deuterium content of water vapor. Atmospheric
870 Measurement Techniques 12, 2331-2339.

871 Yu, W., Tian, L., Ma, Y., Xu, B., Qu, D., 2015. Simultaneous monitoring of stable oxygen isotope
872 composition in water vapour and precipitation over the central Tibetan Plateau. Atmospheric Chemistry
873 and Physics 15, 10251-10262.

874
875